POROSITY PREDICTION IN ALUMINUM A356 ALLOY CASTINGS

A. S. Sabau and S. Viswanathan
Metals and Ceramics Division
Oak Ridge National Laboratory
P.O. Box 2008
Oak Ridge, Tennessee 37831-6083

Abstract

A comprehensive methodology that takes into account alloy solidification, shrinkage-driven interdendritic fluid flow, hydrogen precipitation, and porosity evolution has been developed for the prediction of microporosity fraction in aluminum A356 alloy castings. The mathematical models presented are implemented in a computational framework consistent with those of commercial casting codes, allowing them to be easily incorporated in commercial casting simulation software. Examples are presented for two test-plate castings of vastly differing solidification behavior. The analysis of (a) metallographic observations of the pore morphology distribution, (b) computed solid fraction distribution, and (c) computed pressure distribution during solidification is used to explain the pore fraction evolution during solidification. The predictions of porosity distribution are validated by comparison with independent experimental measurements of pore fraction in the test plate castings.

Introduction

The use of aluminum alloy castings for structural components offers significant opportunities for reducing the weight of automobiles, since aluminum alloy components are typically about half the weight of the steel, cast iron, or ductile iron component that they replace. However, the performance requirements of structural components, particularly chassis or suspension components, places greater requirements on the mechanical properties of the components. An important factor that leads to a decrease in the mechanical properties of castings (notably ductility and fatigue life) is the presence of microporosity.

In the terminology commonly used in the foundry, porosity is usually considered to be either "hydrogen" or "shrinkage" porosity. Hydrogen porosity is the term given to porosity that is generally rounded, isolated, and well distributed. Porosity that is interconnected or clustered, and of an irregular shape corresponding to the shape of the interdendritic region, is usually termed shrinkage. However, in general, the occurrence of microporosity in aluminum alloys is due to the combined effects of solidification shrinkage and gas precipitation (1). Gas pores form when the partial pressure of hydrogen that corresponds to the hydrogen concentration within the liquid exceeds the local pressure in the mushy zone by an amount necessary to overcome the surface energy forces (1). The local pressure in the mushy zone, P_m results from: (a) the ambient pressure, (b) metallostatic head, and (c) resistance to the flow of fluid to feed solidification shrinkage.

Attempts to predict the level of porosity in castings have included both parametric (2-5) and "first-principles" models (1,6,7-11). A number of other studies have also attempted to understand the phenomena of porosity formation, pore growth (12-14), and pore morphology (15).

The governing equations for fluid flow and hydrogen evolution indicate that the porosity formation and fluid flow are strongly coupled. However, in most studies on microporosity (8,13-15), it is considered that the porosity formation does not influence the fluid flow in the mushy zone. Kuznetsov and Vafai (16) showed that neglecting the effect of porosity formation on the pressure in the mushy zone yields lower pressure drops and an over-prediction of final porosity. They also have shown that the influence of porosity formation on the pressure is larger at lower pressures in the mushy zone.

The methodology for microporosity prediction presented in this study allows the numerical simulation of "hydrogen" and "shrinkage" porosity by considering the following factors that contribute to microporosity formation: (a) heat transfer and alloy solidification, (b) microstructure evolution during alloy solidification, (c) hydrogen redistribution during solidification, and (d) fluid flow which feeds the solidification shrinkage. The methodology presented is suitable for easy implementation in commonly used algorithms for fluid dynamics (SOLA and SIMPLE) in commercial and research

software for the simulation of casting processes. The methodology presented has been validated on test castings designed to capture a variety of porosity formation conditions and porosity distributions.

Heat Transfer and Alloy Solidification

Since this work is mainly concerned with the numerical simulation of shrinkage induced flows, the convection term in the energy equation is neglected. The energy equation that describes the heat transfer during alloy solidification appears as:

$$\frac{\partial \overline{\rho h}}{\partial t} + \quad (\rho_l h_l g_l \mathbf{u}) = \quad \left(k_{eff} \quad T\right) \quad , \tag{1}$$

where g_s, g_l, and g_g are the volume fraction of solid, liquid, and gas, respectively; ρ_{se} and g_{se} are the density and volume fraction of the solid eutectic, respectively. $\overline{\rho h} = g_l \rho_l h_l + g_S \rho_S h_S + g_{se}\left(\rho_{se} h_{se} - \rho_s h_s\right)$ is density weighted enthalpy, $\mathbf{u}$ is *intrinsic* fluid velocity, T is temperature, and $k_{eff} = k_s g_s + k_l g_l$ is effective thermal conductivity. Subscripts *s* and *l* refer to the solid and liquid phases, respectively, while subscript *e* refers to the eutectic phases. h_s, h_L, h_g are the intrinsic enthalpies for the solid, liquid and gas phases, respectively. The temperature is solved by the use of an enthalpy formulation (17).

Fluid Dynamics during Casting Solidification

During solidification of alloy castings, regions of solid, mush, and bulk fluid coexist. At low solid fractions, solid nuclei are dispersed in the liquid and carried away by the liquid metal flow. This flow regime in which the alloy behaves like slurry is referred to as mass feeding. At solid fractions larger than a critical value, g_s^{cr}, referred to as the coherency limit, dendrites form a fixed network through which the liquid alloy flows. g_s^{cr} is dependent on the type of alloy and dendrite morphology (18). The flow regime encountered at solid fractions higher than the coherency limit is called interdendritic feeding.

In order to consider the mass and interdendritic feeding, the alloy volumetric fraction, g_c, and alloy density, ρ_c, which are *convected* by the liquid flow are tracked. The g_c and ρ_c variables are given by:

$$g_c = \begin{cases} 1 \text{ if } g_s \le g_s^{cr} \text{ (mass feeding)} \\ g_l \text{ if } g_s > g_s^{cr} \text{ (interdendritic feeding)} \end{cases} \quad . \tag{2}$$

$$\rho_c = \begin{cases} \overline{\rho} \text{ if } g_s \le g_s^{cr} \text{ (mass feeding)} \\ \rho_l \text{ if } g_s > g_s^{cr} \text{ (interdendritic feeding)} \end{cases}$$

The mass conservation equation for the *intrinsic* fluid velocity, $\mathbf{u}$, is given by:

$$\frac{\partial \overline{\rho}}{\partial t} + \quad (\rho_c g_c \mathbf{u}) = 0 \quad , \tag{3}$$

where $\overline{\rho} = \rho_l g_l + \rho_s g_s + g_{se}\left(\rho_{se} - \rho_s\right)$ is the averaged density of the alloy. The solid density, ρ_s, is usually taken to be constant while the liquid density varies with the solute concentration and temperature, $\rho_l = \rho_l(T, C_l)$. The gas density, ρ_g, varies according to the ideal gas law, $\rho_g = P_g / \left(R_{H_2} T\right)$, where R_{H_2} is the hydrogen gas constant.

The momentum equation for the interdendritic flow can be written as:

$$\rho_c \frac{\partial \mathbf{u}}{\partial t} + (\mathbf{u} \quad)\mathbf{u} = - \quad P + \mu \quad ^2\mathbf{u} + \rho_c \mathbf{g} - g_l C_D \mathbf{u} + \mathbf{u} \frac{\partial}{\partial t}\left((1 - g_c)\rho_s\right) \quad . \tag{4}$$

In general, the drag coefficient, C_D, which accounts for the momentum loss due to the flow around and through the dendrite structures, is a function of the velocity magnitude, $|\mathbf{u}|$, permeability, K_S, and liquid fraction, g_l. In this work, the drag coefficient, C_D, is given by the Darcy's and Forchheimer's terms which are often referred to as the "viscous drag" and "form drag" terms (19):

$$C_D\left(|\mathbf{u}|, K_s, g_l\right) = \underbrace{\frac{\mu}{K_s}}_{\text{Darcy's}} + \underbrace{\frac{C_F \rho_c g_l}{\sqrt{K_s}} |\mathbf{u}|}_{\text{Forchheimer's}} \quad . \tag{5}$$

where $C_F = 0.55$.

Permeability in the Mushy Zone

The Kozeny-Carmen equation (20-22) is used to relate the alloy permeability, K_S, to microstructural parameters:

$$K_s = \frac{g_l^3}{k_C S_V^2} \quad , \tag{6}$$

where g_l is the volumetric fraction of the liquid, k_C is the Kozeny-Carman constant, and S_V is the surface area of the solid per unit volume. Based on stereological considerations, S_V is defined as a function of dendrite cell spacing by the following formula:

$$S_v = \frac{4}{d_c} \quad . \tag{7}$$

Microstructural Parameters

In addition to the liquid and solid fractions, which are calculated from the energy equation, the dendrite cell spacing is needed to estimate pore curvature and permeability in the mushy zone. The dendrite cell spacing, d_c, can be correlated with the local solidification time, t_f, by the use of the following relationship:

$$d_c[\mu m] = A t_f^b \quad , \tag{8}$$

where t_f is the local solidification time in seconds. For A356 aluminum alloy, the coarsening constants are determined from published data (23), as:

$$A = 10.2 \text{ and } b = 1/3. \tag{9}$$

For A356 aluminum alloy, the pore radius or curvature, r, is taken to be half of the dendrite cell spacing based on microstructural observations of pore sizes in A356 alloy castings.

Hydrogen Balance

It is commonly accepted that pores form in solidifying aluminum alloys when the equilibrium partial pressure of hydrogen corresponding to the hydrogen concentration within the liquid, exceeds the local pressure in the mushy zone by an amount necessary to overcome surface energy forces (1). Thus, the condition for microporosity formation can be given in terms of a pressure condition:

$$P_g > P_m + P_\sigma, \quad P_\sigma = \frac{2\sigma}{r} \quad , \tag{10}$$

where P_g is the gas pressure corresponding to the gas concentration in the liquid, P_m is the local metallostatic pressure in the solidifying alloy, σ is the surface tension at the gas-liquid interface, and r is the pore curvature. P_σ is the pressure in a pore due to the effects of surface tension.

Equation 10 is only used to provide the condition for a hydrodynamic balance of pressure in the region of a bubble. Since the molten metal used in most foundries has a high concentration of oxide films that serve as nucleating substrates for hydrogen bubble nucleation, detailed models of bubble nucleation may be neglected.

By using Sievert's law to relate the hydrogen concentration in the liquid to the gas pressure, P_g [atm], and neglecting hydrogen diffusion, the hydrogen distribution is described by the following mass balance:

$$f_g C_H^u = C_H^0 - S\sqrt{P_g}\left(f_s k_H + f_l\right) \quad , \tag{11}$$

where C_H^0 is the initial gas concentration within the liquid [cc/100g], S is the hydrogen solubility in the liquid [cc/100g], k_H =0.069 is the partition coefficient for hydrogen distribution between solid and liquid, f_s and f_L are the mass fractions of solid and liquid, respectively. C_H^u is a unit conversion factor from cc/100g to mass fraction (24).

Interdendritic Flow and Microporosity

In order to accurately predict microporosity, a solution algorithm for interdendritic flows in which the coupling between pore growth and liquid feeding is treated implicitly is used in this study. The solution algorithm for interdendritic flows is based on a variable projection method (25) and is extended in this study to include the effect of microporosity on the interdendritic flow. In this methodology, the energy and microporosity equations are uncoupled. The energy equation is solved by using the hydrogen gas fraction at the previous time level, g_g^n, without considering the effect of pore growth within the current time step. $\bar{\rho}^{*n+1} = \rho_l^n g_l^{*n+1} + \rho_s g_s^{*n+1} + g_{se}^{*n+1}\left(\rho_{se} - \rho_s\right)$ is the density which is estimated based on volumetric fractions g_l^{*n+1} and g_s^{*n+1} computed from the energy equation.

An intermediate velocity, **u***, is computed from the momentum equation as:

$$\rho_C\left(\frac{\mathbf{u}^* - \mathbf{u}^n}{\Delta t} + \mathbf{u}\,\nabla\mathbf{u}\right) = \mu\,\nabla^2\mathbf{u}^n + \rho_C\mathbf{g} - \rho_s\frac{\partial g_C}{\partial t}\mathbf{u}^n - g_l C_D\left(|\mathbf{u}^n|, K_S, g_l\right)\mathbf{u}^* \quad . \tag{12}$$

When microporosity is present, the projection step is comprised of the following update of the pressure and velocity:

$$\left(\sigma^{*n+1}\ P^{n+1}\right) = RHS_0 + \left(\frac{\bar{\rho}^{*n+1}}{\Delta t^2} - 3RHS_0\right)\frac{g_g^n - g_g^{n+1}}{1 - g_g^n} \quad , \tag{13}$$

$$g_c^n\rho_c^n\frac{\mathbf{u}^{n+1} - \mathbf{u}^*}{\Delta t} = -\sigma\ \nabla P^{n+1} \quad . \tag{14}$$

where the projection variable and the RHS_0 term are given by:

$$\sigma = \frac{g_C}{1 + g_l C_D \Delta t / \rho_C}, \text{ and } RHS_0 = \frac{1}{\Delta t}\left(\frac{\bar{\rho}^{*n+1} - \bar{\rho}^n}{\Delta t} + \nabla\cdot\left(\rho_c^n g_c^n \mathbf{u}^*\right)\right). \tag{15}$$

In the above pressure relationships, the drag term and projection variable are computed using the liquid fraction g_l^{*n+1} which was computed from the energy equation. Equation 11 is used to relate the last term in Eq. 13 with the pressure. In order to take microporosity effects on the interdendritic flow into account, the last term in Eq. 13 is linearized and the pressure equation is solved iteratively.

Plate Casting

In order to capture the wide range of solidification conditions encountered in sand and permanent mold castings, plate castings were made in a variety of mold configurations. Of those, two castings are of particular interest to this study. They include plates cast in a sand mold and in a sand mold with top, bottom, and end chills. The chill plate configuration is shown in Figure 1. The top and bottom chill dimensions are nominally 200, 150, and 25 mm. The end chill dimensions are nominally 60, 60, and 150 mm. Casting dimensions are shown in Figure 2. All the plates were contained in a sand mold with nominal dimensions of 600, 210, and 200 mm, respectively.

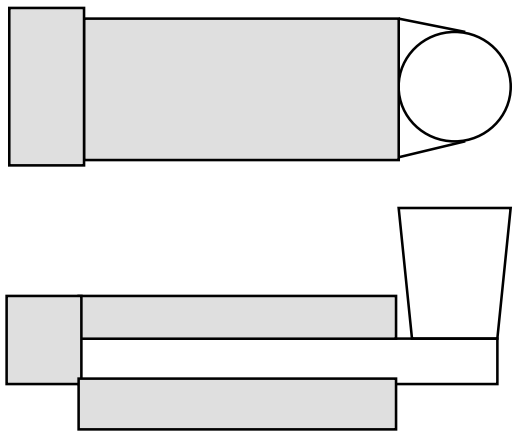

Figure 1: Chill plate configuration.

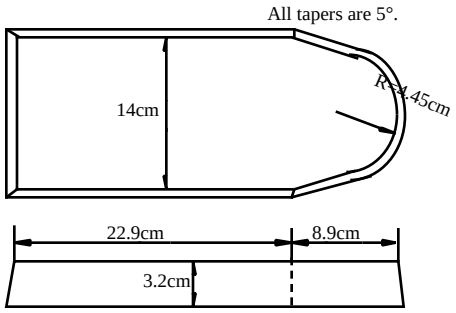

Figure 2: Plate dimensions.

Results and Discussion

Numerical simulation results are presented for A356 alloy sand and chill plate castings. The alloy was poured at 720˚C. The mold-filling phase was neglected in computations, and the initial temperature of the alloy was considered to be uniform over the entire casting. Thermophysical property data were based on experimental measurements and/or data available in the literature. The hydrogen level in the plates was measured to be approximately 0.11 cc/100 g of alloy. The solubility of hydrogen in the liquid phase was determined from data available in the literature for the aluminum-silicon system (26). The evolution of the silicon and magnesium concentrations in the liquid metal as a function of temperature was calculated using the thermodynamic software package ThermoCalc. Due to the symmetry along the vertical section through the plate center, the problem was solved only on half of the plate.

Solidification Behavior

Figure 3 shows the liquid volume fraction distribution for the sand plate and the chill plate, 700 s and 30 s from the onset of solidification. In both plates, solidification progresses from the end of the plate toward the riser without forming any hot spots. In the sand plate, the liquid volume fraction varies from 0 at the end of the plate to 0.7 in the riser [Figure 3(a)]. Although the entire casting is mushy, feeding channels are relatively open as the liquid fraction adjacent to the end of the plate is around 0.5. In addition, cooling rates in the sand plate are small, around 0.1˚C/s, and as a result, the eutectic isotherm velocity is quite small (see Figure 4).

In the chill plate, solidification occurs in the form of a channel that exists over the entire length of the plate [Figure 3(b)]. Also, since cooling rates in the plate are much higher, around 2˚C/s, the resultant eutectic isotherm velocity is also much larger (see Figure 4). In particular, the eutectic isotherm velocity exhibits a maximum in the center of the plate, and this value is almost two orders of magnitude higher than in the edge of the plate.

Figure 5 shows the experimentally determined porosity distribution in the sand and chill plates (27). The porosity level in the sand plate is fairly uniform over the plate and approximately 0.5%. The porosity level in the chill plate, on the other hand, exhibits a maximum at the center of the plate, and this maximum is three times the porosity level in the sand plate. The porosity levels in the sand and chill plates correspond to the profile of the eutectic isotherm velocity in the two plates (Figure 4).

Figure 6 illustrates the pore morphology in two regions of the chill plate. In regions close to the end of the plate and close to the riser, the pores are small and rounded, and are approximately the same size as the local dendrite cell spacing [Figure 6(a)]. In the middle of the plate corresponding to the maximum in porosity, the pores are large, irregular, and conform to the morphology of the interdendritic region [Figure 6(b)]. The pore morphology in the entire sand plate was similar to that in Figure 6(a). In foundry terminology, the pore in Figure 6(a) is considered to be hydrogen porosity, while the pores in Figure 6(b) are considered to be shrinkage porosity.

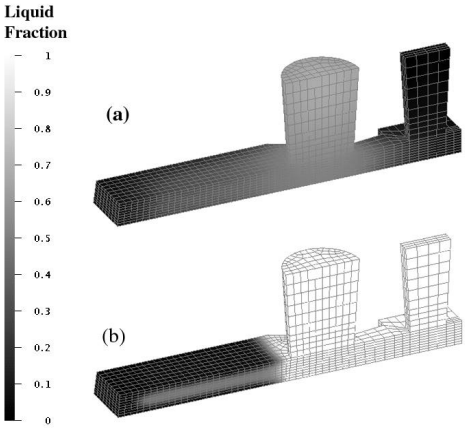

Figure 3: Liquid fraction distribution for (a) sand plate at 700 s, and (b) chill plate at 30 s from the onset of solidification.

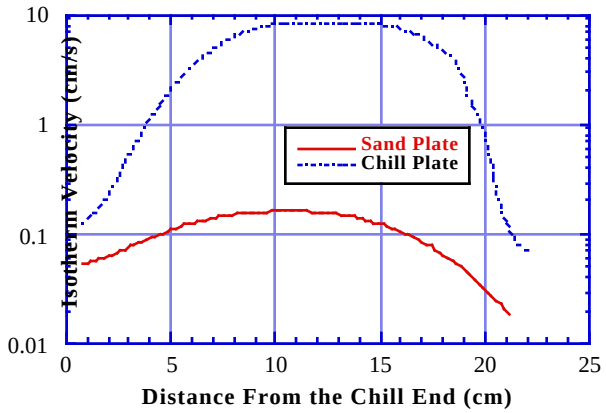

Figure 4: Computed eutectic isotherm velocity for the sand and chill plates.

Pressure Distribution During Solidification

In Figure 7, the evolution of the local pressure in two computational cells is shown as a function of liquid fraction for

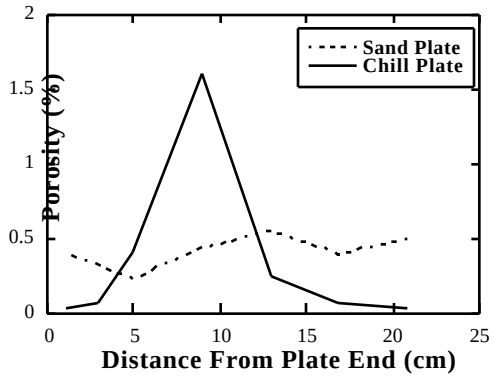

Figure 5: Experimentally measured distributions of pore fraction in the sand and chill plates (27).

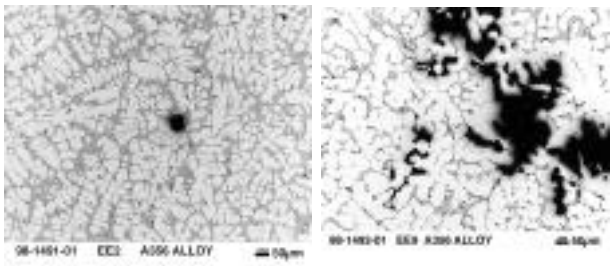

(*a*) (*b*)

Figure 6: Pore morphologies along the centerline of the chill plate casting at locations near the (*a*) plate end (*b*) plate center.

the chill plate. The cells are located along the center of the plate near the end and the middle of the plate. The points correspond to the regions depicted in Fig. 6a and 6b. In regions containing spherical pores, the pressure drop is not significant till the end of solidification. On the other hand, in regions where shrinkage porosity is observed, a severe pressure drop occurs relatively early in the solidification (i.e., at a liquid fraction of 0.5).

Pore Growth during Solidification

A correlation between the computed pressure distribution during solidification and the pore morphologies observed experimentally in the chill plate is used to provide an insight into the pore fraction evolution. As the partial pressure of hydrogen, which corresponds to the hydrogen concentration within the liquid, overcomes the local liquid pressure and surface energy forces, hydrogen porosity nucleates. Immediately following their nucleation, hydrogen pores expand into spherical bubbles that occupy a region between dendrite cells (or between grains). Since this occurs toward the end of solidification, there is little further pore growth, and the final pore size upon solidification corresponds to a radius proportional to the local dendrite cell spacing.

In regions of inadequate feeding, a severe pressure drop occurs early in solidification. This provides the condition for the nucleation of hydrogen, and a bubble is formed. As solidification proceeds, there is further demand for feed metal, but since the resistance to liquid flow is high, the amount of feeding liquid is insufficient to compensate for the entire

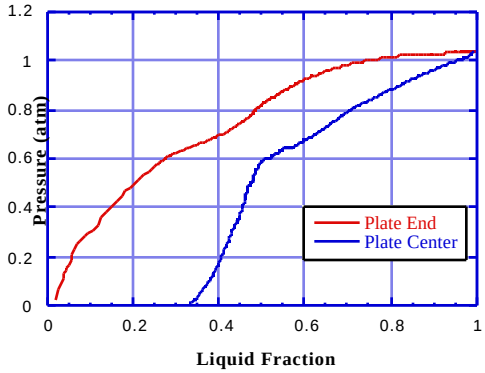

Figure 7: The local pressure distribution corresponding to locations near the plate end and the plate center.

shrinkage. In this instance, the spherical hydrogen pores expand into the irregular interdendritic region as solidification progresses, to compensate for solidification shrinkage. Thus, the categorization of pores as corresponding to hydrogen and shrinkage is actually quite accurate. In the chill plate, both types of porosity are present as the plate contains regions of both good and poor feeding. In the sand plate, the pore morphology at all locations along the plate corresponds to that of hydrogen porosity, as solidification is slow and progressive and no regions of excessive metal demand are encountered.

The above approach was used to model porosity distributions in the sand and chill plates. In regions of severe shrinkage, the *computed* liquid pressure in poorly fed regions can drop below zero absolute pressure. Based on thermodynamic considerations, we consider that the pressure in the liquid is always greater than or equal to the alloy cavitation pressure. If the pressure drops below the alloy cavitation pressure, we consider that liquid feeding ceases and that the solidification shrinkage in that computational cell is compensated only by pore growth.

Figure 8 shows calculated microporosity distributions for the sand and chill plates. The experimentally measured values are also shown for comparison. The agreement for the sand plate is quite good. In the case of the chill plate, the model correctly predicts the maximum in porosity near the center of the plate. However, the predicted minimum porosity is higher, the predicted maximum porosity is lower, and the peak in the distribution is broader than in the experimental results. These differences are attributed to uncertainties in the density values used for the liquid, especially in the region of the final ternary eutectic; the difference in the solubility of hydrogen in complex alloys compared to that in binary alloys; the assumptions in pore radius; and the effects of pore migration during solidification (28).

Summary and Conclusions

A methodology to determine the extent of gas and shrinkage porosity is proposed that is based on thermodynamic considerations and experimental evidence. The solution algorithm presented includes a fully coupled, implicit treatment of local pressure and microporosity evolution in the mushy zone. The methodology presented takes into account alloy

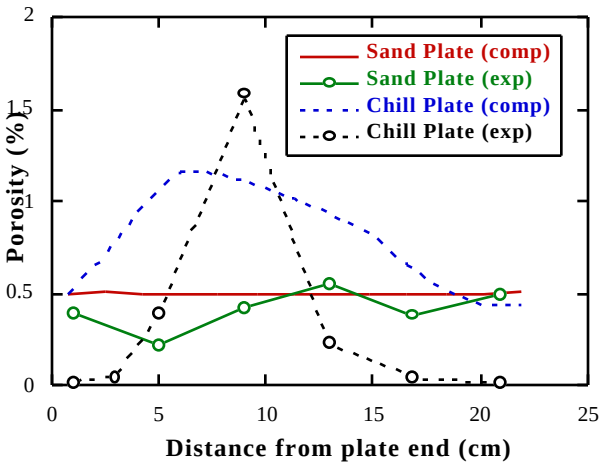

Figure 8: Comparison of experimentally measured and computed porosity distributions along the center of the sand and chill plates.

solidification, shrinkage-driven interdendritic fluid flow, hydrogen precipitation, and porosity evolution during solidification. Microporosity growth is due to the local pressure drop in the mushy zone and pore expansion in casting regions where liquid feeding alone cannot compensate for solidification shrinkage. The solution algorithm presented has been implemented in a computational framework consistent with those of commercial casting codes.

The methodology presented has been validated on test castings designed to exhibit both hydrogen and shrinkage porosity. The numerical results reproduce the characteristic microporosity profiles observed in the experimental results and also agree quantitatively with the experimentally measured porosity levels. The quantitative prediction of porosity levels in production shaped castings provides an enhanced capability for the design of structural safety critical castings.

Acknowledgments

The authors thank D. B. Kothe, Los Alamos National Laboratory, for providing access to the Telluride code for the computations done in this study, Qingyou Han and Ted Huxford for reviewing the paper; and Millie Atchley for preparing the manuscript.

This work was performed under a Cooperative Research and Development Agreement (CRADA) with the United States Advanced Materials Partnership (USAMP), United States Council for Automotive Research (USCAR) for the project on Design and Product Optimization for Cast Light Metals. This research was sponsored by the U.S. Department of Energy, Assistant Secretary for Energy Efficiency and Renewable Energy, Office of Transportation Technologies, Lightweight Vehicle Materials Program, under contract DE-AC05-96OR22464 with Lockheed Martin Energy Research Corp. This research was supported in part by appointments to the Oak Ridge National Laboratory Postdoctoral Research Associates Program, administered jointly by the Oak Ridge Institute for Science and Education and Oak Ridge National Laboratory.

References

1. T. S. Piwonka and M. C. Flemings, *Trans AIME*, Vol 236 (Aug 1966), pp. 1157-65.
2. H. F. Bishop and W. S. Pellini, *Trans AFS*, Vol 58 (1950), pp. 185-87.
3. E. Niyama, T. Uchida, M. Morikawa, and S. Saito, *AFS Int. Cast Metals J.*, Vol 6 (June 1981), pp. 16-22.
4. Y. W. Lee, E. Chang, and C. F. Chieu, *Metall. Trans. B*, Vol 21B (1990), pp. 715-22.
5. S. Viswanathan, V. K. Sikka, and H. D. Brody, *JOM* (Sep 1992), pp. 37-40.
6. W. D. Walther, C. M. Adams, and H. F. Taylor, *Trans AFS*, Vol 64 (1956), pp. 658-64.
7. K. Kubo and R. D. Pehlke, *Metall. Trans. B*, Vol 16B (June 1985), pp. 359-66.
8. D. R. Poirier, K. Yeum, and A. L. Maples, *Metall. Trans. A*, Vol 18A (1987), pp. 1979-87
9. J. Zou and R. Doherty, Modeling of Casting, Welding, and Advanced Solidification Processes VI (TMS-AIME, Warrendale, PA, 1993), pp. 193-200.
10. H. Combeau, A. Bourg, J. Charbonnier, S. Langlois, G. Lesoult, C. Rigaut, and C. Sztur, Modeling of Casting, Welding, and Advanced Solidification Processes VII (TMS-AIME, Warrendale, PA, 1995), pp. 67-75.
11. V. K. Suri and A. J. Paul, *Trans AFS*, Vol 101 (1993), pp. 949-54.
12. Q. T. Fang and D. A. Granger, *Trans AFS*, Vol 97 (1989), pp. 989-1000.
13. S. Shivkumar, D. Apelian, and J. Zou, *Trans AFS*, Vol 98 (1990), pp. 178-904.
14. G. K. Sigworth and C. Wang, *Metall. Trans. B*, Vol 24B (1993), pp. 365-77.
15. J. Huang, T. Mori, and Conley JG, *Metall. Trans. B*, Vol. 29B (1998), pp. 1249-1260.
16. A.V Kuznetsov and K. Vafai, *Int. J. Heat Mass Transfer*, **38**(14) (1995) 2557-2567.
17. A.V. Reddy, D. B. Kothe, C. Beckermann, R. C. Ferrell, and K. L. Lam, Proc. Fourth Int. Conf. on Solidification Processing (The Univ. of Sheffield, U.K., 1997).
18. Arnberg, L., Backerud, L., and Chai, G., *Dendrite Coherency*, **3**, AFS, 1996.
19. Beckermann, C. and Viskanta, R., *Applied Mechanics Reviews*, **46** (1993) 1-27.
20. K. Murakami and T. Okomoto, *Acta Metall.*, Vol 32 (Oct. 1984), pp. 1741-44.
21. D. R. Poirier and S. Ganesan, *Matls. Sci.. Engr. A*, Vol A157 (1992), pp. 113-23.
22. P. Ocansey, and DR. Poirier, *Matls. Sci. Engr.*, **A171** (1993) 231-240.
23. M.C. Flemings, "Solidification Processing," McGraw-Hill (1974) 150.
24. P. Rousset, M. Rappaz, and B. Hannart, *Metall. and Mater. Trans A*, Vol 26A (Sep 1995), pp. 2349-58.
25. A.S. Sabau, Q. Han, S. Viswanathan, Proceedings of Fluid Flow in Metals Processing, TMS Annual Meeting, San Diego, February 28-March 4 (1999a), pp. 403-413.
26. WR. Opie and NJ. Grant, *Trans. AIME, J. Metals*, **188** (1950) 1237-1241.
27. M.D. Dighe, X.G. Jiang, A. Tewari, A.S.B., Rahardjo, A.M. Gokhale, "Quantitative Microstructural Analysis of Micro-Porosity in Cast A356 Aluminum Alloy," Presented at AFS Meeting, Atlanta, 1997.
28. Q. Han and S. Viswanathan, "Pore Migration," unpublished report, 1999.